The Astrophysical Journal, 584:100–109, 2003 February 10

THE GRAVITATIONAL LENS B1608+656. I. *V*-, *I*-, AND *H*-BAND *HUBBLE SPACE TELESCOPE* IMAGING

G. Surpi and R. D. Blandford
California Institute of Technology, MS 130-33, Pasadena, CA 91125; surpi@tapir.caltech.edu, rdb@tapir.caltech.edu
Received 2001 November 6; accepted 2002 October 16

ABSTRACT

We present a multiwavelength analysis of high-resolution observations of the quadruple lens B1608+656 from the *Hubble Space Telescope* archive, acquired with WFPC2 through filters F606W (*V* band) and F814W (*I* band) and with NIC1 in filter F160W (*H* band). In the three bands, the observations show extended emission from the four images of the source in a ringlike configuration that surrounds the two resolved, ensing galaxies. B1608+656 was discovered as a double-lobed radio source and later identified as a poststarburst galaxy in the optical. Based on photometry and optical spectroscopy we estimate that the stellar population of the source has an age of ~500 Myr. This provides a model for the spectrum of the source that extends over spectral regions where no observations are available and is used to generate Tiny Tim point-spread functions (PSFs) for the filters. Deconvolutions performed with the Lucy-Richardson method are presented, and the limitations of these restorations are discussed. $V-I$ and $I-H$ color maps show evidence of extinction by dust associated with one of the lensing galaxies, a late-type galaxy presumably disrupted after its close encounter with the other lens, an elliptical galaxy. The extinction affects the two lens galaxies and two of the four multiple images. The diagnostic of wavelength-dependent effects in the images shows that corrections for contamination with light from the lenses, extinction, and PSF convolution need to be applied before using the extended structure in the images as a constraint on lens models. We will present the restoration of the images in a subsequent paper.

Subject headings: dust, extinction — galaxies: individual (B1608+656) — gravitational lensing
On-line material: color figures

1. INTRODUCTION

The discovery of the first gravitational lens was announced by Walsh, Carswell, & Weymann (1979), long after a number of theoretical papers on lensing had appeared in the 1930s and 1960s. Since then, several consequences of the lensing effect, including strong lensing, weak lensing, and microlensing, have been observed. In a strong lensing situation, a gravitational deflector lying close to the line of sight to a background source creates multiple images of the source. Strong lenses provide a powerful tool to study the distribution of matter, including the dark matter, in the lensing galaxies and to measure the Hubble constant from the time delay between the multiple images (Refsdal 1964). One of the most promising candidates for this analysis is the quadruple lens B1608+656, as a result of the quality of the observations.

The lens B1608+656 was discovered using the Very Large Array during a directed search for radio lenses by the Cosmic Lens All-Sky Survey (CLASS; Myers et al. 1995); 2 months later it was rediscovered in another independent survey aimed at studying faint peaked radio sources (Snellen et al. 1995). The source was found to consist of four flat-spectrum components arranged in a typical "quad" configuration, with a maximum separation of 2.″1 between components. Follow-up optical and infrared observations showed a similar morphology and revealed the lensing galaxy, confirming the lens hypothesis (Myers et al. 1995; Fassnacht et al. 1996). Optical spectroscopy with the Palomar 5 m telescope measured a redshift of $z_l = 0.6304$ for the lensing galaxy (Myers et al. 1995) and gave a redshift of $z_s = 1.394$ for the source, which was also identified as a poststarburst or E+A galaxy (Fassnacht et al. 1996). Monitoring of the radio variability of the source allowed the measurement of the three independent time delays between the components (Fassnacht et al. 1999, 2002).

Several models reproducing the image positions, relative fluxes, and relative time delays in B1608+656 have already been constructed (Myers et al. 1995; Blandford & Kundić 1996; Koopmans & Fassnacht 1999; Surpi & Blandford 2001). One conclusion obtained from these attempts is that modeling of the point-source properties is underconstrained and several solutions are possible (Surpi & Blandford 2001). Additional constraints, from the extended emission of the source, need to be incorporated to break this degeneracy and allow for an accurate lens model and determination of the Hubble constant from the measured time delays.

High-resolution optical and near-infrared imaging of B1608+656 with the *Hubble Space Telescope* (*HST*) has been acquired through four different filters. In this paper we present an analysis of the *V*-, *I*-, and *H*-band archive exposures of B1608+656 from *HST* proposals 6555 and 7422. This set offers a good multiwavelength image sample of B1608+656 in terms of signal-to-noise ratio (S/N). The high resolution obtained in the three bands reveals the extended structure of B1608+656. We compare the images and present a diagnostic of wavelength-dependent distortions in the surface brightness of the source that are superposed on the distortions generated by the gravitational lens deflections. Once identified, the chromatic effects need to be corrected before using the extended emission of the source as a constraint on the lens model. The reconstruction of the images is the subject of a coming paper (G. Surpi & R. D. Blandford 2003, in preparation, hereafter Paper II).

The organization of this paper is as follows. In § 2 we discuss the B1608+656 observations, starting with a summary of the results from radio monitoring in § 2.1, followed in § 2.2 by a report of the optical and infrared exposures already taken with *HST*. In § 3 we comment on qualitative differences among the *V*-, *I*-, and *H*-band images. In § 4 we estimate the age of the poststarburst population in the source and adopt a model for its spectrum. In § 5 we deconvolve the images using Tiny Tim generated point-spread functions (PSFs) and the Lucy-Richardson method for deconvolution. In § 6 we describe $V-I$ and $I-H$ color maps and the evidence of extinction in the system. In § 7 we discuss the properties of the optical and infrared images of B1608+656 and their potential use in the modeling of the lens mass distribution. The Appendix contains details on the processing of the *V*-, *I*-, and *H*-band images.

2. OBSERVATIONS OF B1608+656

2.1. *Radio Properties*

The gravitational lens B1608+656 was discovered with the VLA at 8.4 and 15 GHz by two independent radio surveys in 1994 (Myers et al. 1995; Snellen et al. 1995). The radio images show that the system consists of four well-separated components A, B, C, and D, all of them having flat radio spectra. The radio positions and flux densities of the components, as determined by VLA 8.4 GHz observations of the system (Fassnacht et al. 2002), are listed in Table 1. When a core of 51 mJy is subtracted at 1.4 GHz, the source is a radio galaxy with double-lobed structure having an overall size of $\sim 50''$ and an integrated flux density of 12 mJy (Snellen et al. 1995). The spectrum of the core is flat, while the double-lobe contribution can be modeled with a spectral index of $\alpha = 0.8$ ($F \propto \nu^{-\alpha}$). One of the lobes is highly polarized, while the other one is unpolarized. The core exhibited variability by up to 15% at a frequency of 8.4 GHz, allowing for the possibility to determine the time delays in the system.

A VLA 8.4 GHz monitoring program to determine the time delays of B1608+656 started in 1996. During the first season, the light curve of the components only showed flux density variations at the 5% level. In contrast, during the next two seasons of monitoring the source flux density changed by 25%–30%, experiencing a nearly monotonic decrease during the second season and then an increase during the third one. The combined data from the three seasons allowed us to determine the three independent time delays at the 95% confidence level (Fassnacht et al. 2002), as listed in Table 1.

2.2. *Summary of Optical and Infrared Imaging*

B1608+656 has been observed in the optical and infrared with *HST* in three bands: *V* band (filters F555W and F606W), *I* band (filter F814W), and *H* band (filter F160W), as summarized in Table 2. In this section we compare the sets of observations at each band and identify the best set of exposures in terms of S/N and resolution to perform a multiwavelength analysis of the lens.

The first set of frames in *V* and *I* bands was taken by Jackson in 1996 April, with the Wide Field Planetary Camera 2 (WFPC2), through the filters F555W and F814W (*HST* proposal 5908). These images are presented in Jackson, Nair, & Browne (1997). A second set of exposures in *V* and *I* bands was obtained by Schechter in 1997 November using the WFPC2, through filters F606W and F814W (*HST* proposal 6555). Images in both sets suffer from contamination with cosmic rays and, when the cosmic rays are removed, display noise in the lens region that is dominated by the Poisson fluctuations in the number of counts. In this regime, after combining n frames, the S/N of the resulting image approximately grows as $\propto (nt)^{1/2}$, where t is the exposure time of the frames. Because of their longer exposure time and the larger number of frames, we find that the *V*- and *I*-band images in *HST* proposal 6555 have S/N higher than those in *HST* proposal 5908 by factors of 3.5 and 2.5, respectively.

B1608+656 has also been observed in the infrared *H* band with the Near-Infrared Camera and Multi-Object Spectrometer (NICMOS) of *HST* through the filter F160W. The first observations were taken with NICMOS camera 2 in 1997 September by Falco, for the CfA-Arizona Space Telescope Lens Survey[1] (CASTLES; *HST* proposal 7495). A second set of observations was conducted by Fassnacht in 1998 February, as part of *HST* proposal 7422 (A. C. S. Readhead PI) using NICMOS camera 1. Comparing both sets, as a result of the different pixel size in cameras 1 and 2, the NIC1 frames have resolution higher by a factor of 1.7. On the other hand, NIC2 frames were acquired with dithering that can recover spatial resolution, but sometimes at the expense of creating spatially correlated noise. NIC1 frames have higher background noise compared to NIC2 frames as

[1] The CASTLES gravitational lens database is available at http://cfa-www.harvard.edu/castles.

TABLE 1
RADIO PROPERTIES OF B1608+656

Component	Position[a] (arcsec)	Flux Density[b] (mJy)	Relative Flux[b]	Time Delay[c] (days)
A	(0.000, 0.000)	22.8	2.006 ± 0.014	31.5 ± 3
B	(−0.738, −1.962)	11.6	1.000	0
C	(−0.745, −0.453)	11.6	1.028 ± 0.007	36 ± 3
D	(1.130, −1.257)	3.7	0.342 ± 0.003	77 ± 3

[a] Position offsets with respect to component A in Cartesian coordinates; positive *x*-axis points west.
[b] Results from the third season of VLA monitoring (Fassnacht et al. 2002).
[c] Results of the combined data from three seasons of VLA monitoring; results at the 95% confidence level (Fassnacht et al. 2002).

TABLE 2
OPTICAL AND INFRARED *HST* OBSERVATIONS OF B1608+656

Proposal PI	Proposal ID	Date	Instrument	Filter	Exposures	Exposure Time (s)
N. Jackson	5908	1996 Apr 7	WFPC2	F555W	1	2
					3	500
				F814W	3	800
E. Falco	7495	1997 Sep 29	NIC2	F160W	4	704
P. Schechter	6555	1997 Nov 1	WFPC2	F606W	4	2900
				F814W	1	2800
					3	2900
A. Readhead	7422	1998 Feb 7	NIC1	F160W	5	3840
					1	2048
					1	896

a result of contamination of the lens with the high-noise region of that camera. However, the total exposure time in NIC1 frames is longer by a factor of 8, and this increases the S/N of the combined NIC1 image.

We select the exposures from proposals 6555 and 7422 to perform our multiwavelength analysis in V, I, and H bands, for the following reasons: (1) In V band, the two sets of exposures in filters F555W and F606W are too close in wavelength to provide independent information about extinction, so we take the one with larger S/N. (2) In I band, the combination of the two sets of exposures through filter F814W is not convenient. Because of the relative rotation between the sets, it would be hard to create a combined PSF to deconvolve the combined image. In addition, the information provided by the frames in proposal 5908 would not compensate the error introduced to register them. (3) In H band, NIC1 and NIC2 sets can probably give images of comparable resolution and S/N. Their combination is again not convenient for future deconvolution, and we use the frames in NIC1 here. In summary, the observations that we do not use in this study are entirely consistent with those that we do use but do not improve the S/N.

3. PRELIMINARY ANALYSIS OF V-, I-, AND H-BAND IMAGES

This section presents the results from archival *HST* data of B1608+656 from proposals 6555 and 7422. Exposures include four frames obtained with the WFPC2 through filter F606W (V band), four frames obtained with the WFPC2 through filter F814W (I band), and seven frames obtained with NIC1 through filter F160W (H band). The exposure times are listed in Table 2.

Our goal is to identify qualitative differences between the images and understand their origin. Differences that are not intrinsic to the source but are due to external wavelength-dependent processes, such as extinction or PSF convolution, have to be corrected before incorporating the extended structure of the source and lens galaxies as constraints on the modeling of the system. We want to compare the emission in V, I, and H bands on a pixel-by-pixel basis. Since we are interested in pixel photometry, and not just aperture photometry, we keep the resolution of the images as high as possible. We refer the reader to the Appendix for technical details on the steps followed to process the images with this premise.

Figures 1, 2, and 3 show the V, I, and H images obtained after combining the frames at each band. The images are oriented so that north is up and east is to the left. The intensity is in logarithmic units of nJy pixel^{-1} (1 pixel = 0.″0455), and only fluxes above 3 σ_s are displayed, where $\sigma_s = 1.15$, 0.55, and 6 nJy are the mean standard deviation of the sky noise in V, I, and H bands, respectively. The H-band image is the most affected by PSF convolution, as shown by the clearly defined diffraction rings surrounding components A, C, and D in Figure 3. With a source redshift $z_s = 1.394$, the filters F606W (V band), F814W (I band), and F160W (H band) correspond to source emission at mean rest-frame wavelengths of 2506, 3340, and 6713 Å, respectively. Similarly, for the lens galaxies located at $z_l = 0.63$, we are observing the emission from 3882, 4905, and 9860 Å in their rest frame. The centroids of the four components of the source A, B, C, and D and the lensing galaxies G1 and G2 in each band are listed in Table 6 of the Appendix. Contours of constant S/N for the images are plotted in Figure 4. In general, the V and I bands have approximately the same

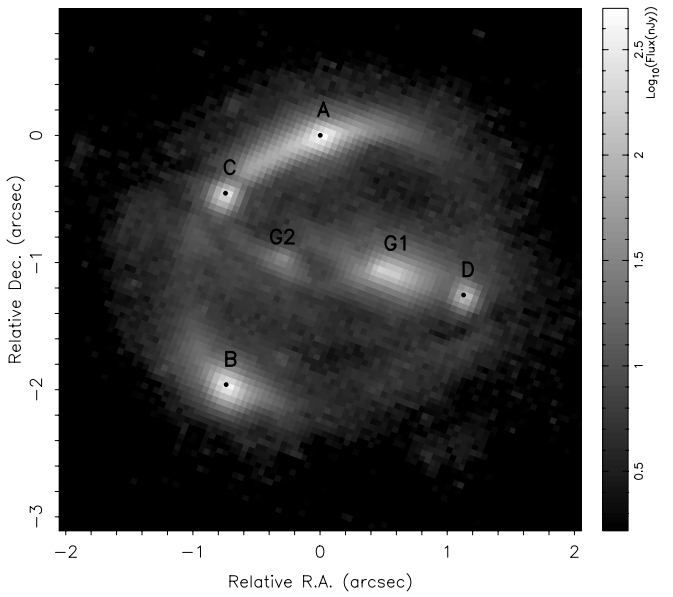

FIG. 1.—V-band image of B1608+656 from F606W exposures by P. Schechter (*HST* proposal 6555). North is up and east is to the left. Image is the average combination of four frames with a total exposure time of 3 hr 13 minutes. Only fluxes above 3 σ of the sky noise are displayed. [*See the electronic edition of the Journal for a color version of this figure.*]

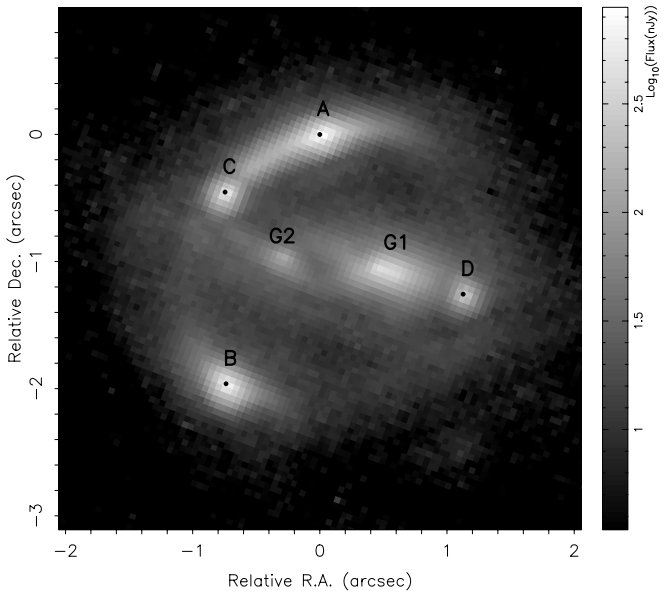

FIG. 2.—*I*-band image of B1608+656 from F814W exposures by P. Schechter (*HST* proposal 6555). North is up and east is to the left. Image is the average combination of four frames with a total exposure time of 3 hr 12 minutes. Only fluxes above 3 σ of the sky noise are displayed. [*See the electronic edition of the Journal for a color version of this figure*.]

level of S/N. Compared to *H*, the S/N in *V* and *I* is higher in low-emission regions. For example, low emission at the 3 σ_s level has S/N $\sim$ 10, 7, and 3 in *V*, *I*, and *H* images, respectively. Isophotes enclosing 50% of the source flux have approximately S/N $\sim$ 30 in the three bands, and isophotes enclosing 10% of the source flux have S/N $\sim$ 70, 70, and 150 in the *V*, *I*, and *H* band, respectively.

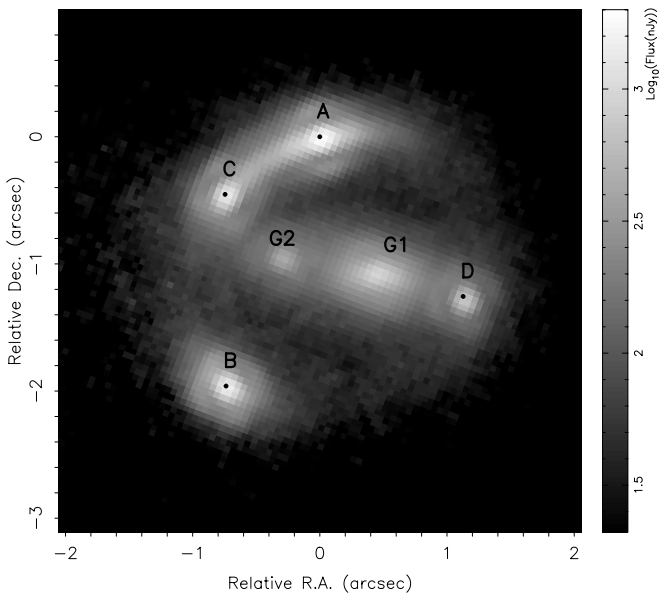

FIG. 3.—*H*-band image of B1608+656 from F160W exposures by C. Fassnacht (*HST* proposal 7422). North is up and east is to the left. Image is the average combination of seven frames with a total exposure time of 6 hr 9 minutes. The ringlike emission at a radius of approximately 0.″23 around each of the multiple images is artificial and caused by diffraction. Only fluxes above 3 σ of the sky noise are displayed. [*See the electronic edition of the Journal for a color version of this figure*.]

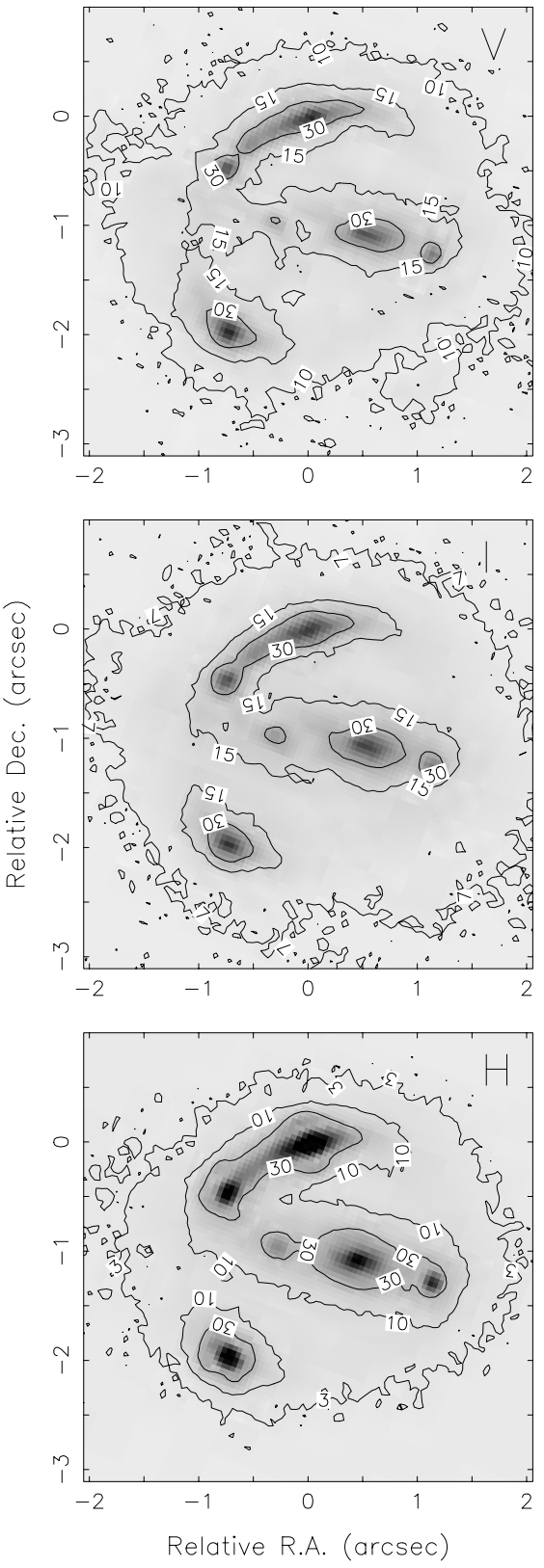

FIG. 4.—Contours of constant S/N in the *V*-, *I*-, and *H*-band images. The emission from the lens has approximately the same S/N in *V* and *I* bands. In the low-emission region, the S/N of *H* is lower than that in *V* and *I* as a result of the high-noise region in NIC1. Displayed contours of S/N $\sim$ 10, 7, and 3 in *V*, *I*, and *H*, respectively, correspond to emission at the 3 σ level. Contours of S/N $\sim$ 30 correspond approximately to isophotes enclosing 50% of the source flux. Peak values of S/N are 90, 85, and 200 for *V*, *I*, and *H* bands, respectively.

All bands reveal the extended structure of B1608+656, showing the four multiple images of the background source embedded in a ringlike emission surrounding the two lens galaxies. There are qualitative differences between the extended emission of the images, however. First, the saddle point that indicates the boundary between C and A images is closer to image C in the V and I bands than in the H band. Since the separation between A and C is determined by the critical curve associated with the lens potential, it should not depend on the wavelength. The shift of $0\farcs16$ in the observed saddle point can be a consequence of extinction, PSF convolution, or a combination of both. If the shift is mainly due to high extinction near C, then the actual saddle point would lie closer to the H location. On the other hand, if the shift is due to the prominent PSF Airy ring in the H band around image C, then the actual saddle point would lie closer to its location in the V and I bands. When the extended structure of the source is incorporated into the modeling of the system (Blandford, Surpi, & Kundić 2001), the saddle points between multiple images (or flux minima in the Einstein ring) can place strong constraints on the lens potential. However, until the images are corrected for extinction and PSF distortions, the uncertainty in the location of the saddle point mentioned above can possibly lead to wrong conclusions if used to constrain or confront lens models as attempted by Kochanek, Keeton, & McLeod (2001).

The second qualitative difference between the images is that the centroid of the lens galaxy G1 appears to shift at decreasing wavelength in, approximately, the west direction. The G1 centroid is displaced by $0\farcs085$ in V band and by $0\farcs073$ in I band, with respect to its H-band location (see Table 6). There are two possible explanations. One is that the east part of the galaxy is being reddened, in which case the G1 centroid would lie closer to its H-band position. The other explanation, proposed by Koopmans & Fassnacht (1999), is that the shift is a consequence of a change in the intrinsic color of G1. These authors propose that dynamical interaction of G1 and G2 could create a bluer region of star formation close to the centroid of G1 in V band and that this centroid would then represent the center of mass of the lensing galaxy. This interpretation supports their best-fitting lens model, which was obtained using the centroid of G1 in V band as a constraint. However, until we understand the origin of the shift of the G1 center as a function of the wavelength, its use to constrain lens models can lead to erroneous conclusions. We should notice at this point that the centroid of G1 is not alone in changing from one band to another; the centroids of G2, D, and C also shift as can be seen from Table 6.

The main conclusion is that a correct interpretation of the features observed in the extended structure of the background source and lens galaxies at V, I, and H bands requires further study of the PSF convolution, intrinsic color variation, and extinction in the system. We discuss these effects in the next sections.

4. SOURCE POSTSTARBURST POPULATION

An optical spectrum of the background source in B1608+656 was obtained with the double spectrograph on the Palomar 5 m telescope by Fassnacht et al. (1996), by positioning the slit so as to minimize the light of the lens galaxies. The spectra showed prominent high-order Balmer absorption lines and Mg II absorption, allowing the determination of a conclusive redshift of $z = 1.394$ for the source and indicating that it is a poststarburst or E+A galaxy. No emission associated with the active galactic nucleus was found. Comparing photometry of the source through the filters F555W, F606W, F814W, and F160W with isochrone synthesis models of Bruzual & Charlot (1993), we find that the poststarburst population in the host galaxy is around 500 Myr old. Figure 5 shows photometry of the B component of the source within an elliptical aperture of radius $0\farcs3$, superposed on the spectrum model. There is a remarkable agreement of the photometry points with the model. The same fit is found for photometry in different areas of B, as this image shows no significant change of color. When the optical spectrum of the source in Fassnacht et al. (1996) is compared with the model, we find that the absorption lines and overall shape of the continuum of the source are fitted well by the 500 Myr old instantaneous burst model of Bruzual & Charlot (1993) as shown in Figure 6, confirming the age estimation.

This model can set an upper limit to the age of the starburst population in the source. Older starbursts would be redder than the source and are ruled out since no mechanism would be able to account for the discrepancies. On the other hand, younger starburst models, if reddened or combined with older stellar components, could still fit the source. We experimented with a younger starburst subject to extinction or superposed on older populations, but the fit to the spectrum and photometry of the source was inferior. We adopt the 500 Myr old instantaneous starburst model to describe the stellar population at the source in what follows. The model provides a synthetic spectrum for the source in the violet end of visible light and infrared where no direct observations are available. The spectrum is used in the next section to generate the PSFs of the V, I, and H filters.

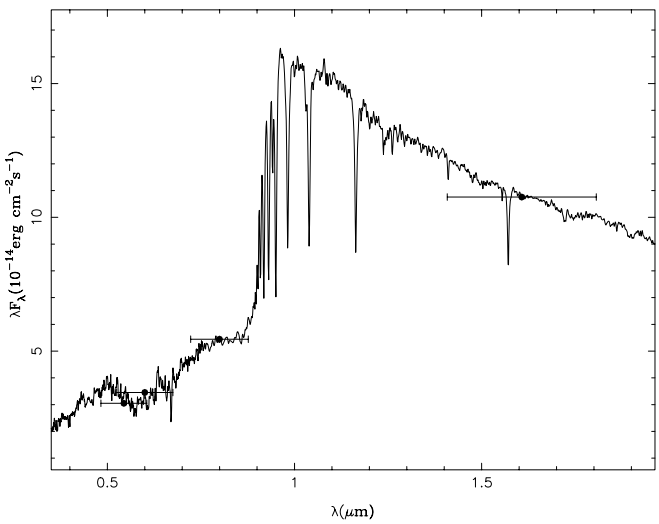

FIG. 5.—Photometry of the B image of the source through filters F555W, F606W, F814W (*HST*, WFPC2, PC), and F160W (*HST*, NIC1). Horizontal error bars show the effective width of the WFPC2 filters and the FWHM of the NIC1 filter. The line shows the 500 Myr old population model from Bruzual & Charlot (1993) redshifted to the observer frame.

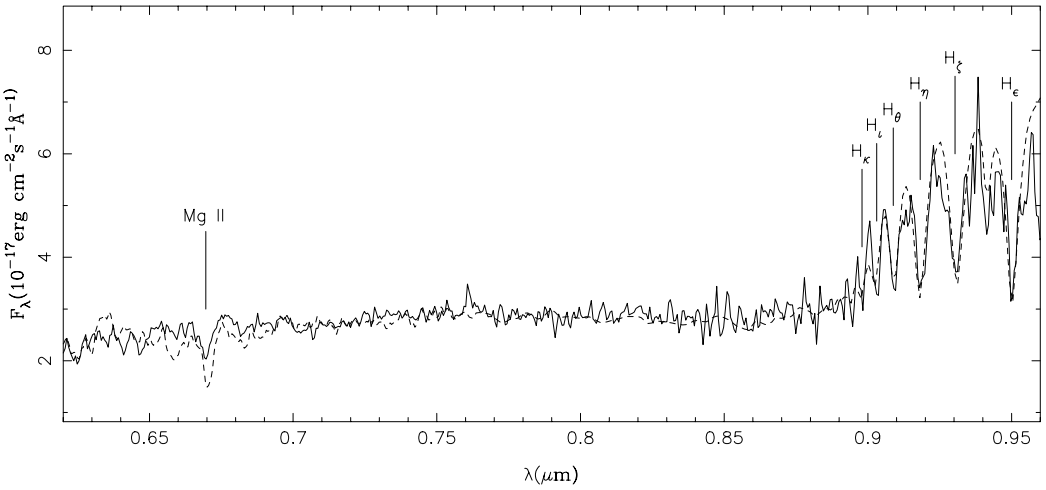

FIG. 6.—Comparison of the optical spectrum of the source in the gravitational lens B1608+656 measured by Fassnacht et al. (1996; *solid line*) with the 500 Myr old population model of Bruzual & Charlot (1993; *dashed line*). Wavelengths are as observed in air. The vertical lines mark the position of the absorption features of the source detected by Fassnacht et al. (1996), which locates it at $z = 1.394$.

5. IMAGE DECONVOLUTION

In this section we present initial deconvolutions of the *V*-, *I*-, and *H*-band images. We use the Tiny Tim software package[2] to generate *HST* model PSFs and the Lucy routine in IRAF (STSDAS)[3] to deconvolve the images. This task restores images using the Lucy-Richardson method (Lucy 1974) adapted for *HST* images contaminated with Poisson noise.

The shape of *HST* PSFs is dominated by diffraction rather than seeing effects. In broadband filters, such as F606W, F814W, and F160W, the generation of the PSFs requires knowledge of both the transmission function of the filter and the spectrum of the observed object. We use the database of wavelength and weights supplied by the Tiny Tim package for the transmission of each filter and the 500 Myr old instantaneous starburst model from Bruzual & Charlot (1993) to characterize the B1608+656 spectrum.

PSFs are constructed with a resolution of 0.″011 by subpixelizing with a factor of 4 in each dimension. We subpixelize the images by the same factor using linear interpolation and deconvolve them with the Lucy routine in IRAF (see footnote 3). The criterion adopted for convergence was to increase the number of iterations until the deconvolved image convolved with the PSF reproduced the observed image within an error of 5%. Many light distributions are, after convolution with the PSF, compatible within a 5% error with the observed image. It is expected then that the difference between the deconvolved image and the original light distribution is higher than 5%. After deconvolution the images were repixelized to their original resolution. The deconvolved images are shown in Figure 7. The *H*-band image is the most difficult one to deconvolve, since the diffraction rings are very prominent. Residuals of the rings are still present around A, C, and D in the deconvolved *H* image. The *H* deconvolution did not solve for the uncertainty in the saddle point between A and C components. The arc in the deconvolved *H* image now shows two minima, one at each side of the intersection between the remnants of the Airy ring around C and the arc. The two locations correspond approximately to the positions of the minima in *V* and *I* and the minima in *H* before deconvolution.

We should stress that, since deconvolution is not a unique operation, the images presented here are the best results obtained under certain limitations: (1) The model assumed for the spectrum is known to fit the observed spectrum of the source, which lies between 6000 and 9600 Å. If the extrapolation of the model toward lower and higher wavelengths has local discrepancies with the spectrum of the source, the restoration in *V* and *H* bands might be limited. (2) The spectrum was assumed constant. It was modeled after the source to obtain better results in the deconvolution of the four images of that object. However, as the result of contamination with light from the lens galaxies and extinction, the color does change across the frame as we will show in the next section. (3) Even for sources of known constant color, deconvolutions are limited by the accuracy of the algorithms used to deconvolve. We tried an alternative deconvolution method, the maximum entropy method (MEM package in IRAF; see footnote 3), and found similar results, except that it produced a slightly higher noise level. The creation of artifacts by the amplification of the noise is the principal illness of the standard methods for deconvolution.

6. EXTINCTION AND COLOR MAPS

The three *HST* images have different angular resolutions because they were convolved with different PSFs during observation. The deconvolution probably has restored the images to comparable resolution but has also amplified their noise. Using the deconvolved images to create the color maps results in maps that are dominated by pixel-scale structure. However, the extinction is an average over a galactic scale length along the line of sight, so it ought to vary relatively slowly across the galaxies. The small-scale

[2] The Tiny Tim User's Guide is available at http://www.stsci.edu/software/tinytim.

[3] The Space Telescope Science Data Analysis System is available at http://stsdas.stsci.edu/STSDAS.html.

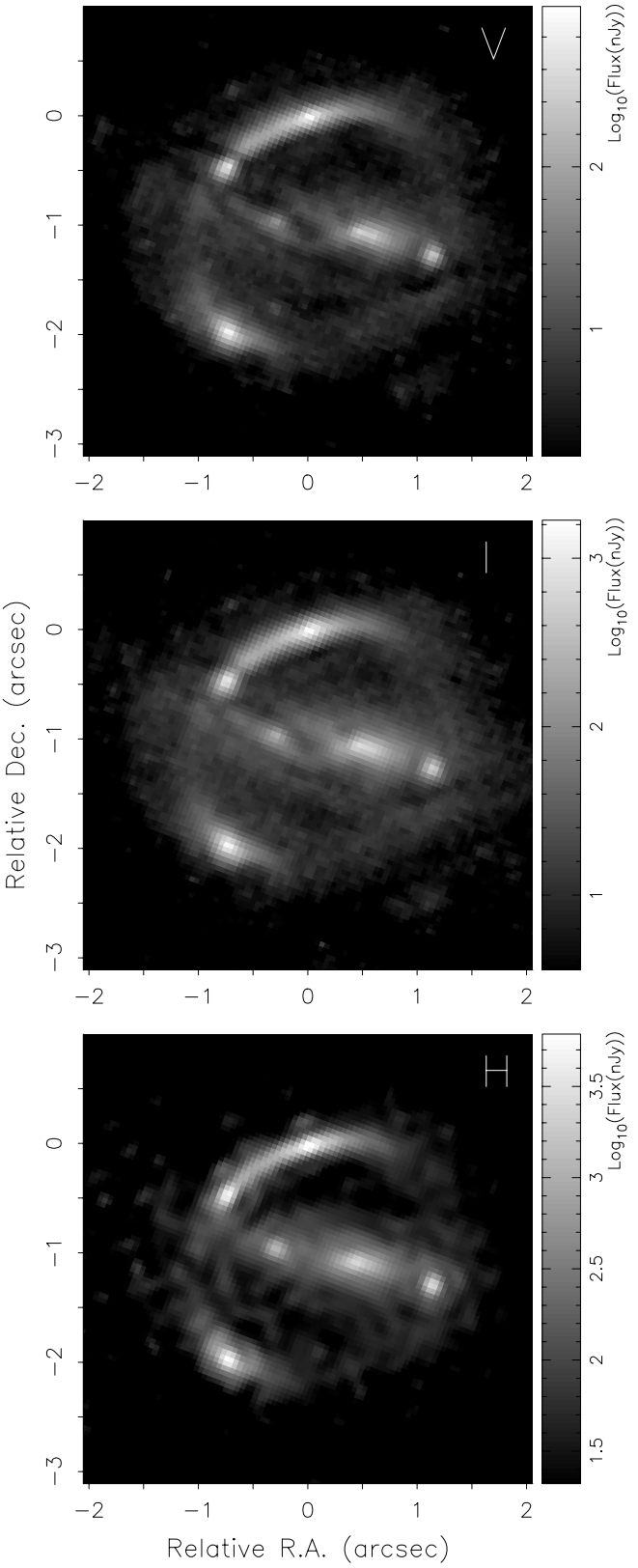

FIG. 7.—Images deconvolved with the Lucy-Richardson method. The gray scale used at each band is the same as in Figs. 1, 2, and 3. The deconvolution has peaked the core fluxes of the source by factors of ~2, 2, and 3 at V, I, and H, respectively. The H image still shows residuals of the Airy rings around images A, C, and D. [*See the electronic edition of the Journal for a color version of this figure.*]

structure observed has to be artificial, as a result of noise that propagates from the deconvolved images. To reduce the noise in the color maps, instead of using deconvolved images, for our analysis we created images of comparable resolution by further convolving each image. At each band we create $\mathrm{PSF_{ratio}} = \mathrm{PSF_{Gauss}}/\mathrm{PSF_{filter}}$, given by the ratio (in Fourier space) between a Gaussian PSF with $\sigma = 1.5$ pixels and the PSF of the corresponding filter. The convolution of the observed images with $\mathrm{PSF_{ratio}}$ results in images of comparable resolution, equivalent to the original images convolved with the Gaussian PSF. In this section we will use V-, I-, and H-band images that have been subjected to this procedure.

A preliminary inspection of the relative magnifications of components A, B, C, and D at H, I, and V bands reveals increasing extinction as we move to shorter wavelengths. We select the $N = 90$ brightest pixels in image B at each band. These pixels are delimited by an isophote of ellipticity 0.34 and semimajor axis of 0.″3 and enclose fluxes of 6.90, 14.5, and 57.6 μJy at V, I, and H band, respectively (which is approximately 50% of the total flux in component B). Since image B is the farthest away from G1 and G2, we assume that it is the least reddened and compute the extinction of A, C, and D relative to B. Assuming that the measured radio flux ratios (listed in Table 1) are correct, we take the brightest N pixels, with $N = 90 \times (2.042,\ 1.037,\ 0.35) = 183.8,\ 93.3,\ 31.5$ for A, C, and D, respectively. These pixels cover matching areas at the source, and their relative fluxes should reproduce, in absence of extinction, the observed radio magnifications. For example, at V band the pixels selected at A should add to flux $F_V(0) = 2.042 \times 6.90\ \mu\mathrm{Jy} = 14.1\ \mu\mathrm{Jy}$. We compute the relative extinction at each component as $A_\lambda = -2.5 \log_{10}[F_\lambda/F_\lambda(0)]$, where $\lambda = H$, I, and V and F_λ is the flux measured in the selected patch. The values are listed in Table 3 and show that A suffers little extinction, while C and D are strongly reddened relative to B.

There are two independent colors, which we choose to be $V-I$ and $I-H$. We use Vega magnitudes $-2.5 \log_{10}(\mathrm{CR}) + \mathrm{ZP}$, where CR is the count rate (measured in units of counts s^{-1}) and the zero point ZP = 21.49, 21.64, and 22.89 for F160W, F814W, and F606W, respectively (STScI 1998). Colors are then evaluated pixel by pixel as $V-I = -2.5 \log_{10}(V/I) + 1.25$ and $I-H = -2.5 \log_{10}(I/H) + 0.15$, where images are in CR units. $V-I$ and $I-H$ colors are shown in Figure 8. The orientation of the color maps is as in Figures 1, 2, and 3.

Color gradients in Figure 8 can arise from two different effects, extinction or variation in the intrinsic color of the objects. At first sight, there is an overall pattern in the color. Both maps show maximum values in a stripe compromising C, G2, G1, and D. A change of color in C and D (with

TABLE 3
EXTINCTION OF THE SOURCE

Parameter	A	B	C	D
A_H	0.08	0.0	0.14	0.20
A_I	0.08	0.0	0.43	0.42
A_V	0.12	0.0	0.69	0.71

NOTE.—Mean extinction relative to B component. The A, C, and D extinctions are measured over areas that match elliptical aperture of 0.″3 in B.

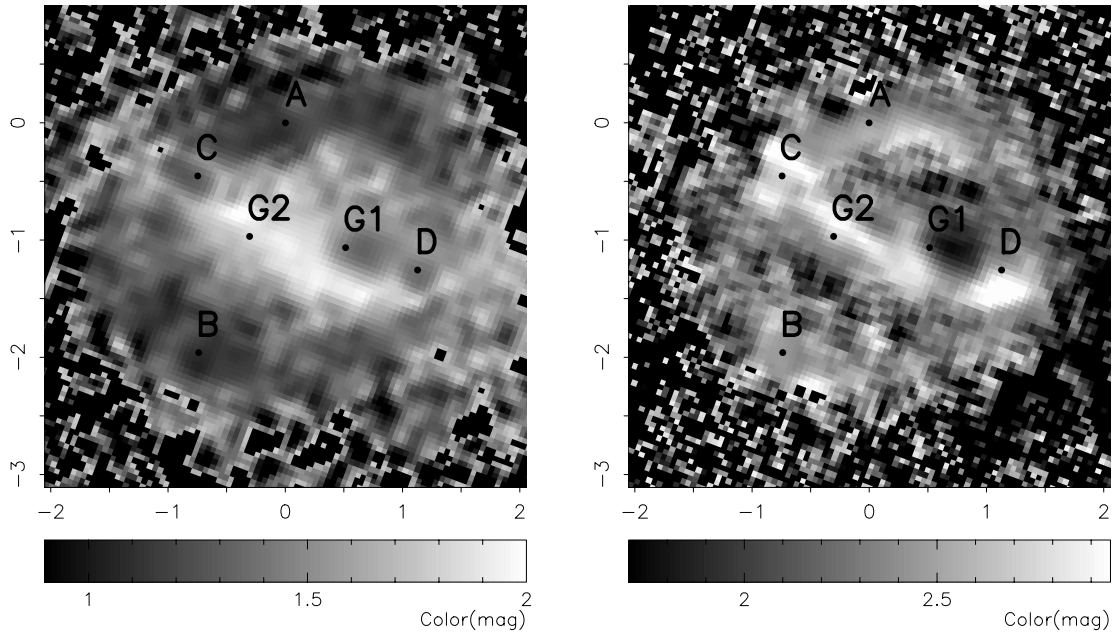

FIG. 8.—$V-I$ and $I-H$ color maps. The orientation of the maps is the same as in Figs. 1, 2, and 3: north is up and east is to the left. V-, I-, and H-band images have been convolved with the ratio between a Gaussian PSF and the PSF of the corresponding filter, to achieve the same resolution before combining them into the color maps. [*See the electronic edition of the Journal for a color version of this figure.*]

respect to A and B) was expected since both images are highly reddened. In G1 and G2, the stripe is broader in the $V-I$ map than in the $I-H$ map, showing that the lenses have different intrinsic color than the source. Contamination of C and D with light from the lens galaxies could also be contributing to their change of color with respect to A and B. Estimated colors within an elliptical aperture of radius 0.″3 in B and matching areas in A, C, and D are reported in Table 4. In the $V-I$ map the color shows larger gradients across the components, and minimum and maximum values are listed in Table 4, while $I-H$ colors reflect average values.

The maps in Figure 8 have color variation across the lensing galaxy G1. There is a minimum of color centered approximately at (0.″7, −1″) and a steep color gradient toward the east direction. Minimum and maximum colors observed in G1 are tabulated in Table 5. The bluer region of G1 does not correspond to the nucleus of the galaxy; it is located 0.″25, 0.″18, and 0.″17 off the centroid of the surface brightness distribution in H, I, and V band, respectively (see Table 6). However, if the two lensing galaxies were interacting dynamically, creating a region of star formation in that area, the change of color could still be interpreted as intrinsic to G1 as suggested by Koopmans & Fassnacht (1999). However, photometry through the bluer window shows that that region is not singular and follows a clearly defined de Vaucouleur profile (Blandford et al. 2001) identifying G1 as an elliptical galaxy. The photometry also indicates that G1 is bluer than the average spectral energy distribution of normal ellipticals (see, e.g., Schmitt et al. 1997). This would agree with the hypothesis of Myers et al. (1995) that the lens might also be a poststarburst galaxy, based on the absorption lines observed in the spectrum. We conclude that the color variations in G1 do not reflect a change of its intrinsic color but differential extinction. The extinction is probably due to dust associated with G2, since ellipticals usually contain little or no dust. On the basis of these color maps we conclude that the dust now associated with G2 must extinguish more than half of the light of G1, implying that the dust is closer to us than G1. Although it is possible to contrive different models, the most natural expectation is that galaxy G2 has a smaller redshift than G1.

The minimum colors quoted in Table 5 for G1 are seen through the lower reddening area and place an upper limit on G1's intrinsic color (a constant reddening over G1 can still be taking place, modifying its photometric color). Combining these values with the maximum colors reported, we estimate G1 color excess $E(V-I) = 0.6$ and $E(I-H) = 1.1$. G1 colors were also extracted by Kochanek et al. (2000);

TABLE 4
SOURCE COLOR

Color	A	B	C	D
$V-I$[a]	1.10–1.50	1.06–1.28	1.28–1.60	1.38–1.51
$I-H$[b]	2.52	2.47	2.70	2.48

[a] Colors are minimum and maximum values measured within an elliptical radial aperture of 0.″3 in B and matching areas in A, C, and D.
[b] Colors correspond to mean values within the same apertures.

TABLE 5
LENS GALAXY COLORS

Color	G1	G2
$V-I$[a]	1.34–1.97	1.67–2.00
$I-H$[a]	1.77–2.87	2.10–2.94

[a] Colors are minimum and maximum values measured.

they found $V-H = 4.48 \pm 0.23$ and $I-H = 2.18 \pm 0.35$ (not corrected for extinction), with V corresponding to F555W. From Table 5 we find mean values $(V-H)_{\rm mean} = 3.97$ and $(I-H)_{\rm mean} = 2.32$. The discrepancy between the $V-H$ values is probably because the V band corresponds to different filters, F606W (here) and F555W (in citation). We do not expect the colors to agree perfectly for two further reasons. First, the G1 color varies across the source, and the average used here might differ from the one used in Kochanek et al. (2000). Second, we estimate colors after convolving the images with the corresponding $\rm PSF_{ratio}$, while in Kochanek et al. (2000) images have not been convolved. We remark that mean colors are not representative of G1 intrinsic color, nor of its reddened color, but just of its average.

In the case of G2, the color also varies across the galaxy. G2's photometric centroid differs in each band; the centroid shifts approximately to the southeastern direction at decreasing wavelength. The I-band centroid is shifted by $0\farcs023$, and V centroid by $0\farcs030$, from the H centroid (see Table 6). This suggests that the extinction is higher in the northwestern part of the galaxy. The color maps in Figure 8 show a redder area located $0\farcs1$ to the right from G2 mean centroid in V, I, and H, likely to be a region of maximum extinction in G2 rather than a redder intrinsic color. We then interpret the variation of color observed in G2 as mainly due to extinction, and once again the minimum and maximum colors observed give indications of the intrinsic color and the most reddened area, respectively. G2 colors are reported in Table 5, and from them we estimate $E(V-I) = 0.3$ and $E(I-H) = 0.8$. Since G2 is abundant in dust, it is probably a late-type galaxy, maybe highly distorted as a result of its encounter with G1.

The color maps shown in Figure 8 have two different sources of error. The first is noise coming from the V-, I-, and H-band images (see Fig. 4). This noise decreases at increasing signal and will mainly compromise the restoration of the low-emission regions. The second uncertainty in the color maps comes from the two PSF convolutions, one during the observation and the second performed here. The noise pattern they produce is opposite to the previous one, with the noise increasing at increasing signal in the images. The degradation due to the convolutions is significant, and the only way of dealing with it is to apply the color maps to images with the same resolution, i.e., images that have been treated with the same convolution process.

7. DISCUSSION

The V-, I-, and H-band *HST* images of B1608+656 show Einstein ring emission from the four images of the radio source, encircling the two lens galaxies. Pixel photometry indicates qualitative differences between the emission in the three bands, arising from extinction and PSF convolution. It is immediately apparent from $V-I$ and $I-H$ color maps that most of the reddening is due to dust associated with the lens galaxy G2, probably a late-type galaxy. The extinction most strongly affects G2, the east portion of the elliptical galaxy G1, and two of the four multiple images of the source, the ones nearly aligned with the position angle of the lenses. Of the three bands, H is the most affected by PSF convolution. The H-band image shows prominent Airy rings around the multiple images and is the most difficult to restore. The H-band image in NIC2, from CASTLES, suffers from the same problem. Additional infrared imaging with the refurbished *HST* or a large ground-based telescope equipped with adaptive optics would be worth pursuing.

There are multiple features that can be seen in the extended emission and used as constraints to break the degeneracy of current lens models: (1) the location and radial profile of the lens galaxies (which are not observed in the radio); (2) special properties of the Einstein ring–like saddle points, traces of the critical curve, and the inner and outer limits where quad images are formed; and (3) the overall ring surface photometry, which satisfies a four-to-one mapping into the source plane. However, the strong extinction in V and I bands, the significant PSF distortion in H band, and the contamination of the ring with emission from the lens galaxies make clear that the images need to be corrected before being used as constraints, or they could lead to misleading conclusions. The multiwavelength strategy required to correct the images will be applied in Paper II, but it can be schematized here based on the observations we made above. First, images have to be taken to comparable spatial resolution. The extinction can then be measured from the color maps constructed with them. If current methods for deconvolution are applied, as these techniques amplify the noise in the images, the deconvolution should be done after the images have been corrected for extinction. PSF deconvolution and the measurement of extinction require knowledge of the intrinsic color of the source and yield better results if applied to a source of constant color, so that a decomposition of the surface photometry into emission from the lens galaxies and the source host galaxy should precede them.

We thank Paul Schechter and Chris Fassnacht for the acquisition of the B1608+656 *HST* data analyzed here and for their encouragement and comments on this manuscript. We thank Eric Agol and Leon Koopmans for discussions and also comments on the presentation that led to an improvement in the manuscript. We are also grateful to Gustavo Bruzual for providing data of the starburst models and Chris Fassnacht for providing B1608+656 spectral data. This material is based on work supported by the NSF under awards AST 95-29170 and AST 99-00866 and NASA under contract NAG 5-7007. G. S. acknowledges support from the CONICET in Argentina.

APPENDIX

IMAGE PROCESSING

We first estimated the mean sky level at each frame and subtracted it. In addition, in the H frames we also subtracted a sky gradient, originated by the propagation of the high-noise region of NIC1 in the lens area. We then proceeded to register the frames. Only one geometrical transformation was performed in each frame. The V- and I-band frames were registered by means of shifts. As the H frames had smaller pixel size and were rotated with respect to V and I frames, a general geometrical

TABLE 6
CENTROIDS

Parameter	*V* Band (arcsec)	*I* Band (arcsec)	*H* Band (arcsec)
A	−0.0049, −0.0032	0.000, 0.0000	−0.0015, −0.0094
B	−0.7377, −1.9646	−0.7382, −1.9614	−0.7393, −1.9617
C	−0.7555, −0.4612	−0.7499, −0.4586	−0.7419, −0.4496
D	1.1250, −1.2568	1.1250, −1.2534	1.1261, −1.2767
G1	0.5266, −1.0664	0.5137, −1.0639	0.4414, −1.0754
G2	−0.3121, −0.9722	−0.3045, −0.9696	−0.2931, −0.9489
δ(A)	0.0035, 0.0020	0.0027, 0.0015	0.0016, 0.0010
δ(B)	0.0028, 0.0025	0.0022, 0.0020	0.0014, 0.0014
δ(C)	0.0034, 0.0033	0.0024, 0.0024	0.0015, 0.0016
δ(D)	0.0050, 0.0049	0.0034, 0.0035	0.0020, 0.0021
δ(G1)	0.0063, 0.0031	0.0040, 0.0022	0.0026, 0.0016
δ(G2)	0.0012, 0.0098	0.0062, 0.0050	0.0032, 0.0028

NOTE.—The values at each band give the position offset with respect to component A in *I* band measured in Cartesian coordinates with the positive *x*-axis pointing west. Centroids and errors were determined from images in Figs. 1, 2, and 3 using the IMCENTROID routine (see footnote 3).

transformation was applied to register them. We point out that only the centroids of components A and B were used to register the frames in different bands because, as we saw in § 6, the centroids of C, D, G1, and G2 can be apparently displaced as a result of extinction. After masking bad pixels (in *V*, *I*, and *H* frames) and cosmic rays (in *V* and *I* frames), we finally used averages, with weights reflecting the exposure times, to combine the frames at each band. The resulting images are shown in Figures 1, 2, and 3. The locations of the centroids of the four images of the sources A, B, C, and D and of the two lens galaxies G1 and G2 at each band are shown in Table 6.

We then evaluated the S/N in the images on a pixel-by-pixel basis. In the *V* and *I* images the noise was estimated from contributions of Poisson, readout, and background noise. In *H* band the background noise changed from frame to frame, and also across each frame, so we determined the noise using the dispersion of the data at each pixel. The S/N contours are shown in Figure 4.

REFERENCES

Blandford, R. D., & Kundić, T. 1996, in The Extragalactic Distance Scale, ed. M. Livio, M. Donahue, & N. Panagia (Cambridge: Cambridge Univ. Press), 60
Blandford, R. D., Surpi, G., & Kundić, T. 2001, in ASP Conf. Ser. 237, Gravitational Lensing: Recent Progress and Future Goals, ed. T. G. Brainerd & C. S. Kochanek (San Francisco: ASP), 65
Bruzual, G., & Charlot, S. 1993, ApJ, 405, 538
Fassnacht, C. D., Pearson, T. J., Readhead, A. C. S., Browne, I. W. A., Koopmans, L. V. E., Myers, S. T., & Wilkinson, P. N. 1999, ApJ, 527, 498
Fassnacht, C. D., Womble, D. S., Neugebauer, G., Browne, I. W. A., Readhead, A. C. S., Matthews, K., & Pearson, T. J. 1996, ApJ, 460, L103
Fassnacht, C. D., Xanthopoulos, E., Koopmans, L. V. E., & Rusin, D. 2002, ApJ, 581, 823
Jackson, N. J., Nair, S., & Browne, I. W. A. 1997, in Observational Cosmology with the New Radio Surveys, ed. M. Bremer, N. Jackson, & I. Perez-Fournon (Dordrecht: Kluwer), 315
Kochanek, C. S., Keeton, C. R., & McLeod, B. A. 2001, ApJ, 547, 50
Kochanek, C. S., et al. 2000, ApJ, 543, 131
Koopmans, L. V. E., & Fassnacht, C. D. 1999, ApJ, 527, 513
Lucy, L. B. 1974, AJ, 79, 745
Myers, S. T., et al. 1995, ApJ, 447, L5
Refsdal, S. 1964, MNRAS, 128, 307
Schmitt, H. R., Kinney, A. L., Calzetti, D., & Storchi Bergmann, T. 1997, AJ, 114, 592
Snellen, I. A. G., Bruyn, A. G., Schilizzi, R. T., Miley, G. K., & Myers, S. T. 1995, ApJ, 447, L9
STScI 1998, *HST* Data Handbook 3.1, chap. 28, Table 28.1
Surpi, G., & Blandford, R. 2001, in ASP Conf. Ser. 237, Gravitational Lensing: Recent Progress and Future Goals, ed. T. G. Brainerd & C. S. Kochanek (San Francisco: ASP), 413
Walsh, D., Carswell, R. F., & Weymann, R. J. 1979, Nature, 279, 381